# Comparison of Hall-Petch Law with an Elastic Limit Identification Method Using Kinematic Field Measurements

Q Hu, A Beaurain, J F Witz, A El Bartali, D Najjar

# Comparison of Hall-Petch Law with an Elastic Limit Identification Method Using Kinematic Field Measurements

Q. Hu[1*], A. Beaurain[1], J.F. Witz[1], A. El Bartali[1], D. Najjar[1]

[1]Univ. Lille, CNRS, Centrale Lille, UMR 9013-LaMcube-Laboratoire de Mécanique, Multiphysique, Multiéchelle, Villeneuve d'Ascq, 59655, France

[*]Corresponding author: Q. HU, qi.hu@centralelille.fr

## Abstract

**Background** Plastic deformation in polycrystalline metals is highly heterogeneous due to the varied microstructure distribution. Although some traditional laws, such as the Hall-Petch law, describe the relationship between microstructure and yield stress, accurately predicting the initial yield stress (hence elastic limit) related to local plasticity activation remains challenging.

**Objective** This study proposes a novel approach to identify local elastic limits using full-field strain measurements, avoiding complex constitutive models.

**Methods** Full-field kinematic measurements were performed on the heat-treated polycrystalline 316L austenitic stainless steel. By examining the different mechanical responses during elastic and plastic deformation, the onset of plasticity activation for each grain is identified from its grain-average strain evolution, allowing further calculation of the grain-scale elastic limit.

**Results** Strain field observations indicate early strain localizations, particularly at twin boundaries and triple junctions. Based on microstructures segmented by ordinary grain and twin boundaries, considering and not considering twins, two different local elastic limits are identified.

**Conclusions** The average elastic limit for the case considering twins is closer to the value obtained from the macroscopic stress-strain curve. In addition, the statistical analysis of the classified grain sizes reveals a more pronounced Hall-Petch relationship when twins are considered. These results indicate the necessity of considering twins in identifying the local mechanical properties.

**Keywords** Polycrystal; Kinematic fields; Hall-Petch law; Plasticity activation; Microstructure

## 1. Introduction

It is well known that the macroscopic mechanical response that controls the mechanical properties of a material originates from the microstructure. During the mechanical loading, the deformation field of polycrystals is usually highly heterogeneous due to their varying grain size, morphology, and crystallographic orientation. The influence of microstructural features on heterogeneous deformation or localized plasticity has been investigated in many experimental and numerical studies [1-5]. Usually, plasticity occurs gradually when a material is subjected to a stress beyond its yield stress. Several phenomenological models have been proposed to determine this macroscopic yield stress, including one based on the thermal effects induced during mechanical loading and the widely recognized Hall-Petch law related to the average grain size of materials. The thermal variation-based method to determine the activation of plasticity was first proposed in [6], where the yield stress is defined at the transition between thermoelastic and thermoplastic regimes. However, due to very low temperature variations during quasi-static deformation processes and the high diffusivity of metals, the experimental determination of plasticity activation and yield stress at the local scale from this perspective is laborious and complicated [7].

In addition, the well-known empirical Hall-Petch law connects the macroscopic yield stress of the bulk material to its average grain size [8, 9]: $\sigma_y = \sigma_0 + k_{HP} d^{-1/2}$, where $\sigma_y$ is the yield stress of the material, $\sigma_0$ is the lattice friction stress, $d$ is the grain size, and $k_{HP}$ is the Hall-Petch coefficient. This relationship has been successfully validated in many single-phase metals, as presented in reviews [10-12].

Since its proposition, various models have been developed to explain the physics of grain size effect associated with deformation mechanisms, where the most commonly applied model is the dislocation pileup model [13, 14]. Although the Hall-Petch relationship has been incorporated into numerous simulation studies to address the influence of grain size [3, 15-17], its applicability in illustrating the correlation between grain size and local plasticity on a microstructure scale remains uncertain, especially considering the heterogeneous distribution of grain sizes within the aggregate. This is because the grain size effect in polycrystals is a macroscopic manifestation derived from the statistical analysis of local results. For an individual grain, its yield stress is influenced not only by its own size, shape, and orientation but also by interactions with neighboring grains, which are inherently difficult to quantify or measure. Moreover, the yield stress is classically defined by a 0.2% strain offset on a stress-strain curve, even if the plasticity is activated before this conventional point. Therefore, the macroscopic Hall-Petch relationship is not prudent for estimating the initial yield stress locally (hence the elastic limit where the stress-strain curve becomes nonlinear) corresponding to the activation of plasticity [18].

With the application of full-field measurement techniques, such as digital image correlation (DIC), the deformation mechanisms from the bulk specimen to the local zone and even to the activation of slip systems have been studied in depth [19-22]. It provides rich experimental data (local displacement and strain fields) for gaining insight into and characterizing the mechanical behavior of materials at the microstructure scale. Combined with finite element simulations, heterogeneous elastoplastic properties of the

material, including elastic limit and hardening modulus, can be identified by solving inverse problems [23-28]. In contrast to previous studies, which require a large number of experimental datasets and complex constitutive laws for simulation, this paper proposes an alternative method for identifying local elastic limits through the elastic/plastic strain partitioning through the full-field measurements. This straightforward method is a phenomenological approach that does not rely on a complex constitutive model. Furthermore, it is based on direct and precise measurements of the strain fields and avoids strong assumptions and quantification of specific microstructure parameters.

After the previous introduction, this paper is organized as follows. The first part describes the test conducted and characterizes the microstructure of the specimen within the region of interest (ROI). In the second part, the full-field strain fields for the whole ROI are discussed. Afterward, the strategy to identify the onset of plasticity activation and then the local elastic limit at the grain scale is presented, based on the distinction between elastic and plastic regimes from the full-field measurements. Finally, with the help of microstructure segmentation, a statistical analysis of the identified grain-scale elastic limits is conducted, where the results are classified by grain sizes, both with and without consideration of twins.

## 2. Material and methods

### 2.1. Specimen preparation and experimental methodologies

The studied material is an AISI polycrystalline 316L austenitic stainless steel. The dog-bone-shaped specimen was extracted from a steel plate along the rolling direction

by wire electrical discharge machining. The specimen geometry and dimensions are shown in Fig. 1(a), with the gauge area of 10 mm×7 mm×2 mm. A relatively short gauge length was chosen to ensure that the onset of plasticity could be captured within the camera system's field of view (details of the camera system will be described in the last paragraph of this section). The as-received specimen underwent an annealing heat treatment at 1200 ºC for 3 h in a vacuum, followed by furnace cooling, which increased the mean grain size from the original 15 μm to 250 μm (measured by the slope-intercept method without considering the annealing twins) to facilitate the measurements at the grain scale. The chemical composition of the annealed material, as measured by glow discharge optical emission spectroscopy (GDOES), is presented in Table 1. The results are in good agreement with the specifications outlined in ASTM A240[1]. The edges and both surfaces of the specimen were finely polished to 2000 particle size with silicon carbide grinding papers. Then, the observed surface was further polished up to 1 μm with a diamond suspension, followed by electrochemical etching (with the solution of 50% Nitric acid) at 10 volts and a current density of 30 $mA/cm^2$ for 1 minute at room temperature. The ROI of about 6.6 mm×5.7 mm is located in the center of four small Vickers indentations, which serve as fiducial markers for image repositioning. A contrasted speckle pattern for the DIC calculation was prepared by covering calcium carbonate particles on the surface of a uniform black matte paint primer using an airbrush.

The test was performed on an electro-mechanical Instron 5580 testing machine,

[1] ASTM A240, Standard Specification for Chromium and Chromium-Nickel Stainless Steel Plate, Sheet, and Strip for Pressure Vessels and for General Applications

under displacement control with a cross-head speed of 1 mm/s, corresponding to a strain rate of $2 \times 10^{-3} s^{-1}$. Fig. 1(b) shows the macroscopically monotonic stress-strain curve of the studied specimen subjected to uniaxial loading at room temperature. The engineering stress is determined by dividing the force of the load cell by the initial section of the gauge area. The axial strain is calculated by averaging the results obtained by using the DIC technique over the ROI. The stress exhibits a linear variation with the strain until point A, which can be considered to be the elastic limit (124 MPa) of the material. Before the occurrence of linear hardening (CD) attributed to the generalized plasticity, the material undergoes an elastoplastic transition (AB) related to the plasticity of some favorably oriented grains. Moreover, the increase in grain size through heat treatment results in yield stress at 0.2% plastic strain offset for the current specimen (205 MPa), which is lower than that of the standard 316L stainless steel (261 MPa) [29], aligning with the description from the Hall-Petch relationship.

| Component | C | Si | Mn | P | S | Ni | Cr | Mo | N |
|---|---|---|---|---|---|---|---|---|---|
| ASTM A240 | <0.03 | <0.75 | <2 | <0.045 | <0.03 | 10~14 | 16~18 | 2~3 | <0.1 |
| GDOES | 0.011 | 0.336 | 1.12 | 0.035 | 0.009 | 10.209 | 15.924 | 2.017 | 0.164 |

Table 1 Comparison of certified chemical compositions and GDOES measurements of an annealed 316L austenitic stainless steel (weight %)

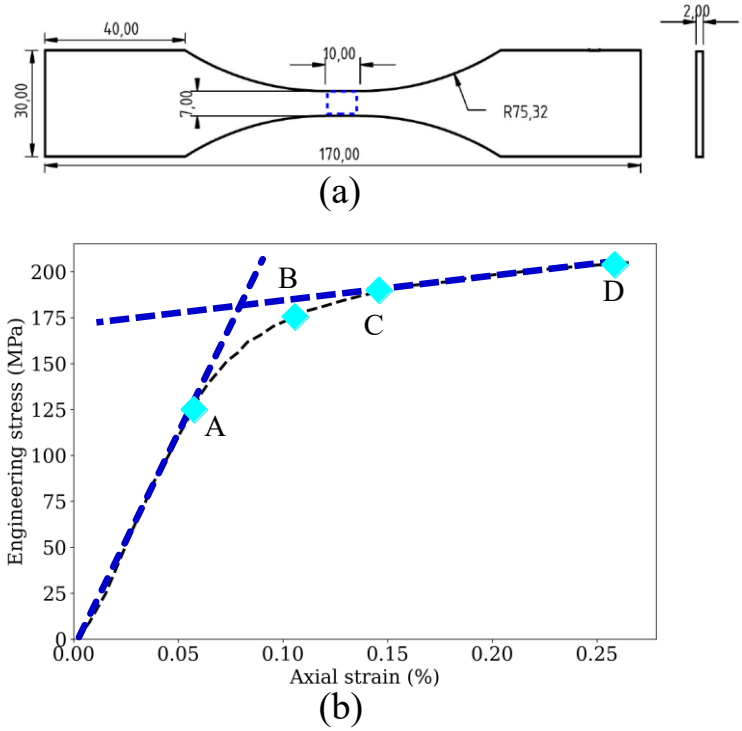


**Fig. 1** (a) The geometrical dimension of the studied specimen, (b) Evolution of the macroscopic engineering stress-strain during the loading stage

Full-field kinematic measurements were performed on the homemade YaDICs platform [2, 30] based on the finite element global method, with the element size chosen as 16 pixels×16 pixels. The coarse-to-fine approach is applied to speed up the algorithm, with a median filter of radius of 3 at each level. Under the small deformation assumption, the engineering strain components are computed from the numerical gradients of the in-plane displacement fields, specifically: $\varepsilon_{xx} = \frac{\partial u}{\partial x}$, $\varepsilon_{yy} = \frac{\partial v}{\partial y}$, and $\varepsilon_{xy} = \frac{1}{2}(\frac{\partial u}{\partial x} + \frac{\partial v}{\partial y})$. The equivalent von Mises strain under the plane strain assumption is calculated with the following formula: $\varepsilon_{vm} = \sqrt{\frac{4}{9}\left(\varepsilon_{xx}^2 + \varepsilon_{yy}^2 - \varepsilon_{xx}\varepsilon_{yy}\right) + \frac{4}{3}(\varepsilon_{xy}^2)}$. Using an appropriate lens and camera for image acquisition is necessary to achieve a high spatial resolution and ensure reliable DIC calculations on the microstructure scale. In the current work, an XIMEA CB500 camera with a 7920×6004 pixels sensor was paired

with a LAOWA 25mm f/2.8 2.5-5X Ultra-Macro lens at a magnification of X2.5, resulting in a pixel size of 1.84 μm. In order to increase the frequency of image acquisition, the images were cropped to 5400×4800 pixels, providing a field of view of 9.9 mm×8.8 mm, ensuring that all free surfaces of the ROI are captured within the image. The analyses in the following parts are based on the actual strain fields measured using DIC within the ROI. Therefore, the applicability of St. Venant's principle to the designed specimens was not specifically considered. The DIC calculations result in a spatial resolution of about 30 μm×30 μm for the kinematic fields with the chosen element size. The uncertainty of the strain measurements can be evaluated by rigid-body translations before the test, allowing for an assessment of the entire measurement chain. In the in-plane rigid body translation test with an axial displacement of 100 μm, the strain error is about 0.02%. The out-of-plane rigid body translation test with a displacement of about 30 μm presents a strain error of about 0.06%. It can be observed that the out-of-plane effect has a relatively significant impact on measurement errors, particularly when utilizing a high-magnification lens.

### 2.2. Microstructure characterization

The highlighted microstructure by etching within the ROI was characterized by optical microscopy (OM) before and after the test. A series of images with an overlap of 20% were taken at X50 magnification and stitched in the NIS-Elements software, which covers the whole ROI with a pixel size of 0.68 μm. Fig. 2(a) shows the microstructure of the investigated specimen before the test. The image segmentation on the microstructure was first performed using the MorphoLibJ module in Fiji [31], which

allows the skeleton of the grain boundaries to be automatically extracted. However, due to the incomplete closure of etching grain boundaries and the influence of noise, image segmentation generally cannot be fully automated. The previous skeletons were further manually modified in ImagePy [32], where the missing grain boundaries were manually completed. Fig. 2(b) displays the results obtained by automatic segmentation with manual modification.

After the removal of the speckle pattern with acetone and ethanol in the ultrasonic water bath, the deformed microstructure within the ROI was characterized using electron backscatter diffraction (EBSD). Considering that the final deformation of the specimen was relatively small, less than 2%, one assumes that the crystal orientations of the specimen after deformation represent those before deformation [33]. EBSD measurements were conducted by a Hitachi scanning electron microscope（SEM) system equipped with an Oxford EBSD detector. The acquisition was carried out at an accelerating voltage of 20 KV and a working distance of 10 mm. EBSD scans were acquired at X33 magnification with a step size of 2 μm. A total of 25 maps were obtained with an overlap of 15%. Before repositioning and stitching them into the DIC reference system, the optical distortion of these EBSD scans was corrected using thin plate spline transformation. The detailed procedure is described in reference [2]. Fig. 2(c) and (d) represents the inverse pole figure (IPF) mapping from the X-Y plane of specimen within the ROI that has been repositioned in the reference framework, and the standard triangle respectively. Grains are color-coded with respect to the Z axis, which is perpendicular to the observed surface.

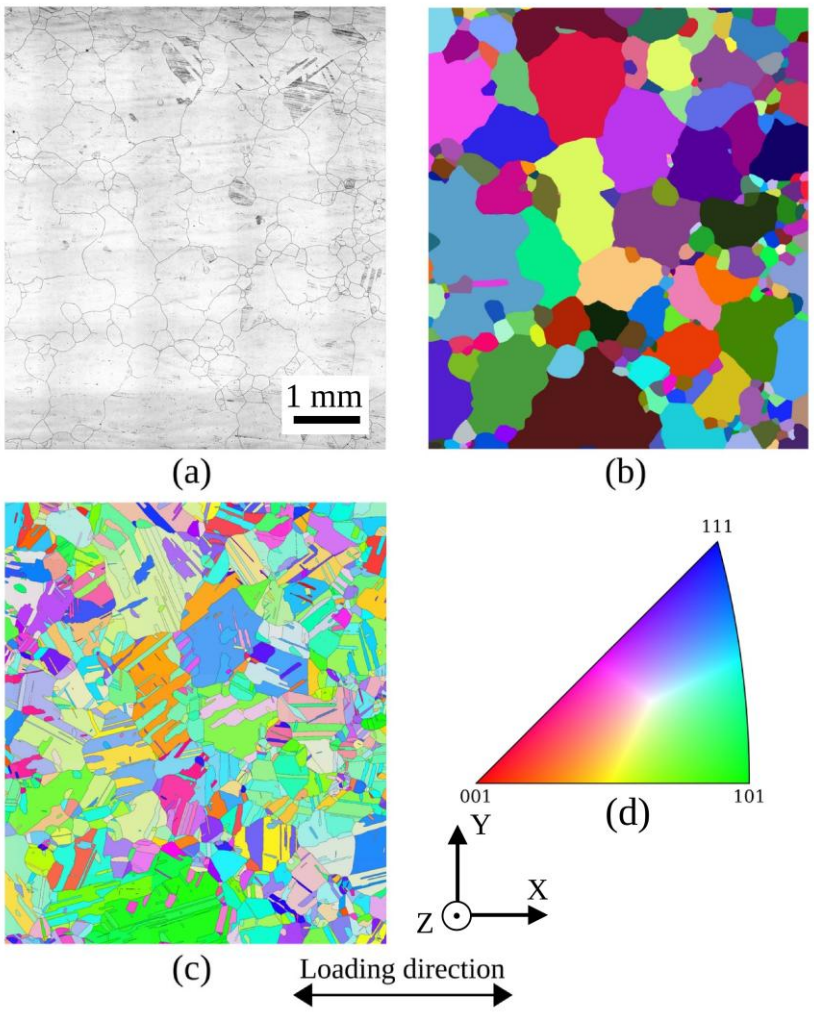


**Fig. 2** (a) The microstructure within the ROI of the studied specimen before the test, (b) the segmented microstructure, (c) IPF with respect to the Z axis, and (d) the standard triangle for the representation of grain orientations

Fig. 3 shows two different patterns of grain boundaries obtained: ordinary grain boundaries where the misorientation is larger than 10° (depicted by the black line) and twin boundaries where crystal lattices are related by a 60° rotation (indicated by the brown line). This yields two different grain distributions i.e., including and excluding twins, in terms of numbers and average grain sizes. Ordinary grain boundaries identify 331 grains with equivalent diameters ranging from 18 to 1845 μm. These grains present an average size of $d_{exc}$=273 μm. Conversely, twin grain boundaries identify a larger

number of grains, 1449 in total, but with a narrower range of grain sizes from 18 to 1015 μm and with the average grain size reducing to $d_{inc}$=137 μm.

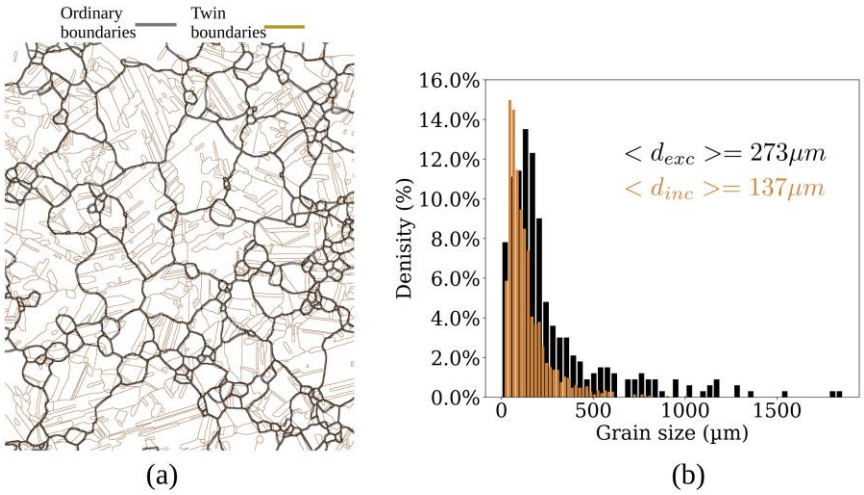


**Fig. 3** (a) Ordinary grain boundaries (in black lines) and twin boundaries (in brown lines), (b) Grain size distribution obtained by segmented images

The out-of-plane displacement due to plastic deformation was characterized by the height distribution on the deformed surface using a Veeco Wyko NT 9300 profilometer with a measured step of 1.6 μm. The height distribution represented in the non-deformed configuration is shown in Fig. 4(a), which ranges from -7 to 9 μm with an average value of 2 μm. Considering a mirror-like polishing up to 1 μm on the measured surface was conducted before the test, thus the heterogeneities of height distribution are due to the out-of-plane movements resulting from plastic deformation along the Z axis. Fig. 4(b) shows the resulting strain due to the out-of-plane displacement after the test, which is quantified by the gradient of height [2]:

$$\nabla Z = \sqrt{\left(\frac{\partial Z}{\partial x}\right)^2 + \left(\frac{\partial Z}{\partial y}\right)^2}$$

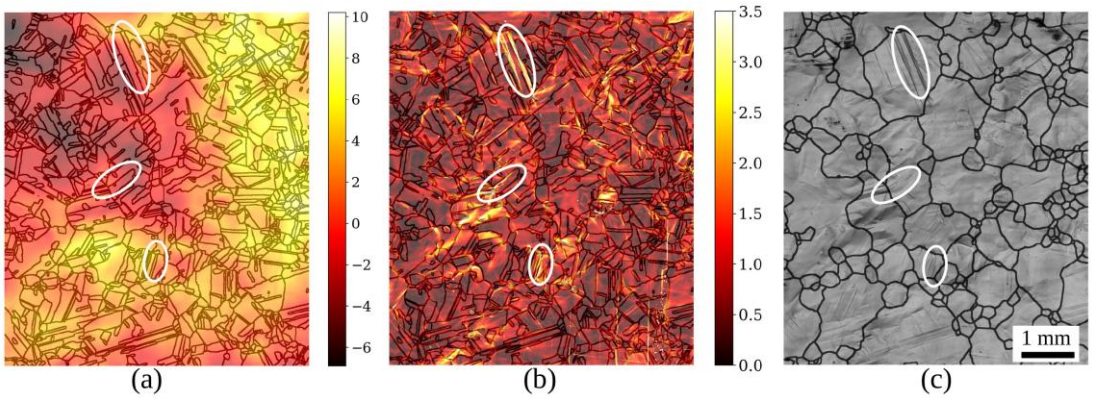


**Fig. 4** (a) Profile maps of the deformed surface, in units of μm, (b) Gradient of the height on the deformed surface, in units of %, represented in non-deformed configuration and superimposed with ordinary grain and twin boundaries, (c) Microstructure of the deformed surface superimposed with ordinary grain boundaries

Compared to the microstructure after the test in Fig. 4(c), the heterogeneous distribution of the height gradient is in good agreement with the discontinuities of the microstructure. Most of the pronounced heterogeneities are located on or near the twin boundaries, as shown by the white ellipses, which emphasize the link between microstructural discontinuities and heterogenous localization around ordinary grain and twin boundaries.

## 3. Results

### 3.1. Evolution of strain fields measured by DIC

The equivalent von Mises strain fields at specific moments, corresponding to the points A, B, C, and D on the macroscopic stress-strain curve in Fig. 1(b), are highlighted and presented in Fig. 5. The average values of these strain fields are 0.06%, 0.13%, 0.21%, and 0.29%, respectively. The grain boundaries with a width equal to the element size for DIC calculation, that is 16 pixels, are superimposed. The white bidirectional arrow represents the loading direction of the specimen. Limited to the uncertainty of

the DIC calculation, the field in Fig. 5(a) is significantly influenced by the noise. In particular, several artifacts result from the shedding of speckles at the beginning of loading, which are evident at the initial loading and then become less visible as the physical strain increases, as highlighted in the blue boxes. The first strain localizations can be observed in Fig. 5(b), as indicated by the blue arrows. These heterogeneities are located near the grain triple junctions and extend along the grain boundaries. Notably, a clear example is indicated by the blue arrow in the middle left part of Fig. 5(b). With the increase of applied stress, plastic strain gradually accumulates around the initial localizations, resulting in the formation of more extensive localization zones at the same positions, as shown by the yellow ellipses in Fig. 5(c). New localizations gradually emerge as the average strain increases, primarily located near grain boundaries, indicated by the green arrows in Fig. 5(c) and (d). In addition, in grains with extensive deformation, the incompatibility of deformation at the boundaries extends into the grain, generating intragranular strain localizations, as indicated by the yellow arrows in Fig. 5(c). The spatial distribution of the strain field in Fig. 5(d) remains almost consistent with the previous state, except that the intensity of these localizations increases monotonically with the increasing stress.

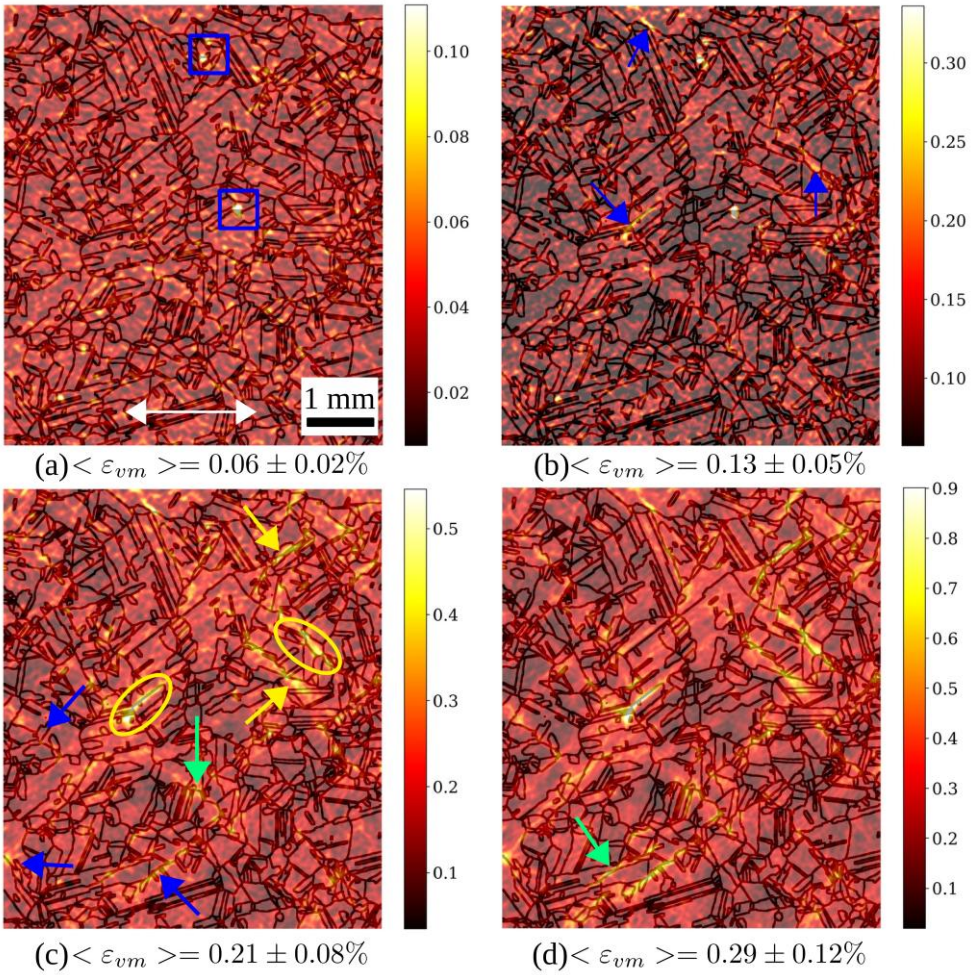


**Fig. 5** Equivalent von Mises strain fields (in %) corresponding to the points (a) A, (b) B, (c) C and (d) D on the macroscopic curve

These observations reveal the spatial and temporal heterogeneities in plastic strains. For a polycrystalline metal, these heterogeneities arise from microstructural heterogeneities such as grain orientation, shape, and size, which could reflect the heterogeneous distribution of the elastic properties of the material. In the following section, the method for identifying elastic limits on the grain scale based on the evolution of the full-field strain fields measured by DIC is presented, which encompasses two cases, with and without considering twins. The identified elastic limits are further subjected to statistical analysis.

### 3.2. Identification of elastic limits at the grain scale

The mechanical behavior of the material transitions from elasticity to plasticity due to the differences in modulus. During the elastic regime, Hooke's law, which relates to Young's modulus and Poisson ratio, describes the mechanical behavior of isotropic elastic materials. Conversely, a hardening modulus with an appropriate hardening law is required in the plastic regime to characterize the mechanical response accurately. Basically, the material undergoes recoverable elastic deformation with a linear strain evolution over time until the loading reaches the elastic limit. Once local plasticity occurs, the material's response deviates from linearity, manifesting an elastoplastic transition followed by a progressive hardening regime. This difference in mechanical behaviors between elastic and plastic regimes allows for determining the bulk elastic limit from the macroscopic stress-strain curve. However, the local elastic properties of materials are heterogeneous due to variations in crystallographic characteristics such as grain size, morphology and orientation, as well as the influence of surrounding grains. Using the engineering stress measured by the load cell to identify the local elastic properties related to the plasticity activation becomes inaccurate. As a result, this work proposes a method for identifying the elastic limit for each grain based on the evolution of experimentally measured local strain by DIC as the function over time rather than relying on stress.

In the test controlled by displacement with a constant loading rate, the strain increases linearly with time until the onset of plasticity, where the applied stress exceeds the elastic limit or the plasticity is activated. The elastic limit can then be determined

using Hooke's law, based on the measured strain at the onset of plasticity. Therefore, accurately determining these moments of plasticity activation is crucial for identifying the local elastic limit. One feasible method is to perform segmented linear regression on the measured strain evolution and calculate the coefficient of determination ($R^2$ values) between the fitted and measured curves. In an ideal case, where strain measurements are not affected by the noise, the segmented linear regression on the elastic strain data will show a high correlation, with $R^2$ values close to 1. When plasticity is activated, this correlation decreases; hence, the rapid drop in $R^2$ value is considered an indication of the onset of plasticity, as shown in Fig. 6(a). However, in real strain measurements, the effect of noise is unavoidable, particularly when the strain is small. This results in lower $R^2$ values even during the purely elastic strain regime, which gradually increase with the number of fitted points and reach a maximum value after the activation of plasticity, as shown in Fig. 6(b). Based on these observations, the procedure of the proposed method for detecting the onset of plasticity for each grain is as follows:

1. Obtain curves of the mean strain evolution over time for each grain;

2. Perform the linear regression to the first $n$ measured strain points ($n$>4);

3. Incrementally increase the number of points and calculate the $R^2$ value between these strain data and their linear regression;

4. Determine the moment, i.e., $t_{el}$, when the maximum or local maximum value of $R^2$ exists. The elastic limit corresponds to the stress calculated by Hooke's law at $t_{el}$, $\sigma_{el}^{g} = E\varepsilon^{g}(t_{el})$.

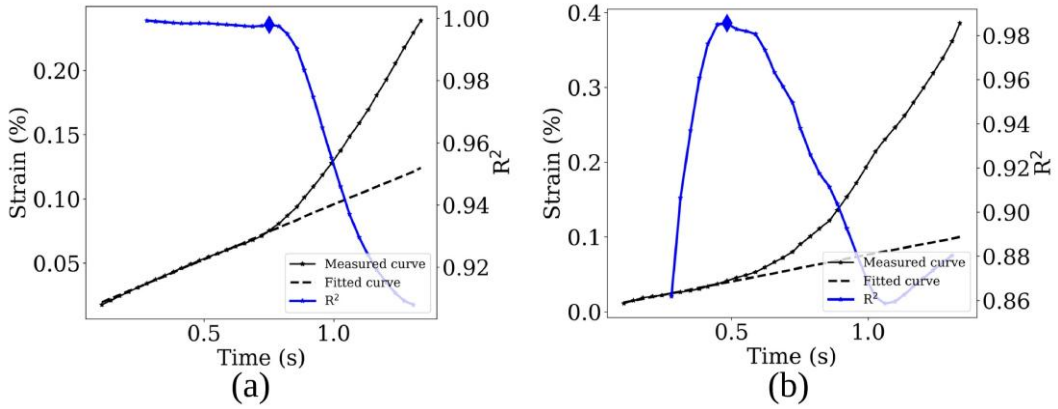


**Fig. 6** Examples of determining the plasticity activation for the grains (a) without noise effects, (b) with noise effects

The above procedure of identifying the elastic limit was performed on the segmented microstructure in Section 2.2, including the cases considering twins or not. However, the proposed method for the elastic limit identification may not be valid for grains with sizes smaller than the spatial resolution of the applied DIC technique (i.e., 30 μm), where the measurement of the strain is seriously affected by the noise. Therefore, such small grains are not taken into account during the identification process. For the case with consideration of twins, a total of 21/1449 grains were excluded, which accounts for 1% of the ROI in terms of number and area. In the case without consideration of twins, a total of 10/331 grains are excluded, which occupies approximately 3% of the total number of grains and represents only about 0.6% of the area of the ROI. In terms of numbers and areas, removing these grains does not affect the statistical analysis of the results.

Fig. 7(a) and (c) present the identified elastic limits for all grains, with mean and standard deviation values of 129±45 MPa (with twins) and 95±30 MPa (without twins), respectively. The average values of the identified elastic limits for all grains are

calculated by considering the volume fraction $f_g$ of each grain. The calculation is performed using the following formula:

$$< \sigma_{el} >= \sum f_g \sigma_{el,g}$$

where $\sigma_{el,g}$ is the identified elastic limit of each grain. Assuming a uniform size distribution of grains along the thickness (Z axis), the volume fraction is calculated as $f_g = \frac{S_g}{S_{total}}$, where $S_g$ is the area of grain $g$, and $S_{total}$ is the total area of the ROI.

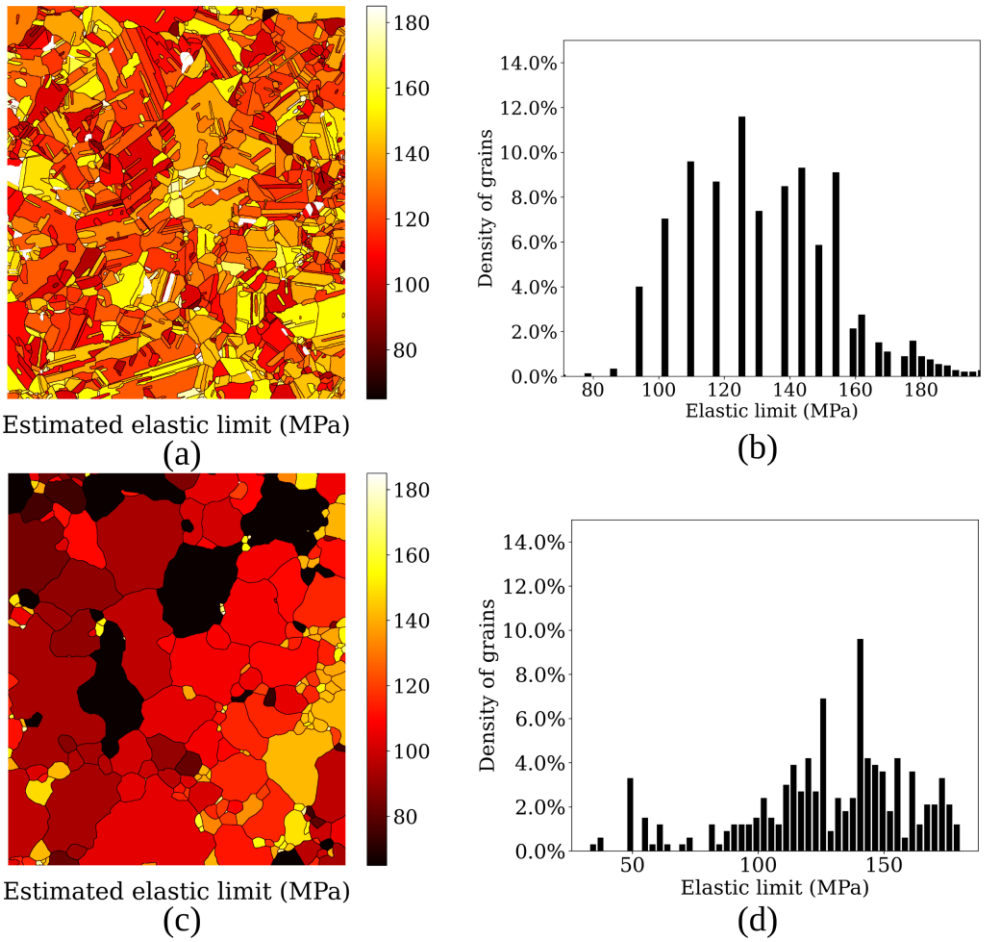


**Fig.** 7 Identified elastic limit fields for all grains (a) with and (c) without considering twins. The histograms of grain-scale elastic limits (b) with and (d) without considering twins

The mean elastic limit when considering twins is closer to the macroscopic one (124 MPa) determined from the macroscopic curves. In addition, the histograms of the identified elastic limits in Fig. 7(b) show that the distribution considering twins presents

a Gaussian pattern, which is physically meaningful and reflects the combined effects of factors like grain size and orientation, as described by the central limit theorem.

### 3.3. Classification of grains

Considering the different average grain sizes (137 μm including twins and 273 μm excluding twins), the mean value of the identified elastic limits is higher when twins are taken into account. This seems to be in agreement with the Hall-Petch relationship. This observation prompts us to analyze locally whether a similar Hall-Petch relationship exists between the grain sizes and the identified grain-scale elastic limits in the previous section. Fig. 8 illustrates the distribution of the elastic limits that satisfy the identification conditions within the ROI as a function of their grain sizes. One could observe that, due to the dispersion of the identified elastic limits, the Hall-Petch relationship is not evident by directly observing these two distributions, especially when considering the presence of twins.

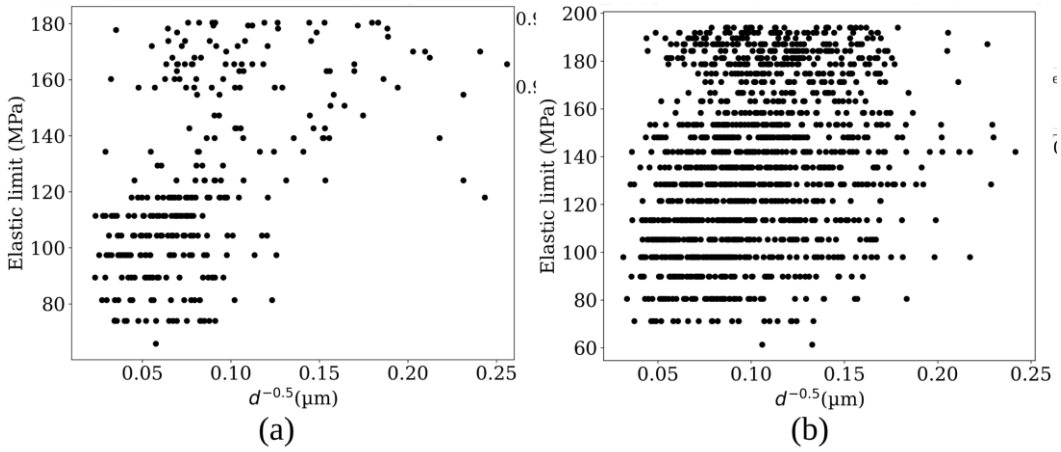


**Fig. 8** Distribution of grain-scale elastic limits as the function of grain size (a) excluding twins, (b) including twins

In order to perform statistical analysis from these inconclusive data, the reduction

of correlation scatter was achieved by classifying the grains within the ROI into several different categories based on size. The mean values of grain sizes and identified elastic limits were then calculated for each classification to evaluate the presence of the Hall-Petch relationship. Given the Gaussian-like distribution of the grain sizes and identified elastic limits, as well as the moderate number of grains, this study applies Sturges' Rule to determine the number of classifications [34], which is expressed by the following formula:

$$k = 1 + \log_2 N$$

where $N$ denotes the total number of data points, and $k$ represents the number of classifications. To facilitate a more intuitive comparison, the number of classifications is kept consistent across both cases of considering twins or not. Using the same number of classifications ensures a uniform standard, which allows for a more accurate comparison of distribution characteristics. The calculation of this number is based on the grain count from the case without considering twins (331), resulting in at least 9 classifications according to the previous formula. Considering the small number of grains with a size larger than 600 μm, the grains exceeding this value are classified into a single category. The remaining grains are then classified into $k-1$ groups with equal intervals, where the average grain size and elastic limit are counted. Afterward, a linear regression is performed on these data points, and the $R^2$ values between the data points and their linearly fitted curves are calculated for different numbers of classifications. As shown in Fig. 9, $R^2$ values decrease with the increasing number of classifications. In order to reduce the dispersion of the statistical results without

affecting their plausibility, we set the $k = 9$, which provides sufficiently high $R^2$ values for both cases, whether considering twins or not.

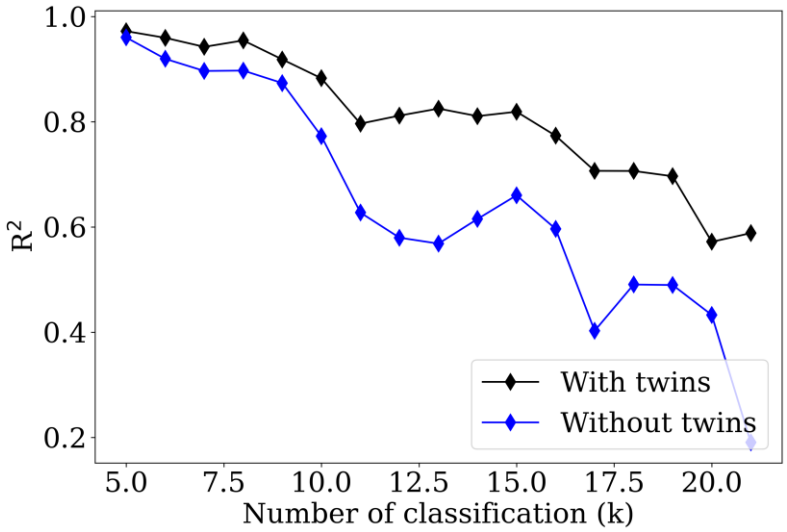


**Fig. 9** $R^2$ values between the data points and their linear fitting curves for different numbers of classifications

### 3.4. Investigation of Hall-Petch relationship based on grain classification

The results of identified elastic limits and grain sizes ($d^{-1/2}$) for the classifications of grains are presented in Fig. 10(a). A linear regression is then performed to fit the data, resulting in the black and blue curves corresponding to the cases with and without considering twins, respectively. The high $R^2$ values between the fitted curves and the data points suggest that both curves exhibit the typical Hall-Petch relationship, indicated by the increase in elastic limits with $d^{-1/2}$. The $R^2$ value between the fitted curve and calculated data for the case with considering twins is larger than the one without consideration of twins. Moreover, the less scattered distribution of black points validates the importance of twins in establishing the Hall-Petch relationship.

It can be observed that the intercepts (depending on the lattice friction) of the two

Hall-Petch curves are different. The twin boundaries could act as barriers for dislocation movements for a polycrystal, even if they are usually considered low-energy boundaries [3]. Due to the presence of the boundaries, dislocations arriving at a grain boundary cannot freely cross the boundary. Therefore, the material with higher boundary density tends to exhibit a higher elastic limit. This is reflected in the larger intercept, $\sigma_0$, for the results with twins compared to the ones without twins.

Fig. 10(b) compares the Hall-Petch relationship for the case with twins from current work with those from other studies [35-38]. The grain size strengthening factor (slope) aligns well with reported values (300–600 $MPa \cdot \mu m^{-0.5}$), but the intercept is relative lower. This difference stems from the fact that previous studies use the yield stress at a 0.2% plastic strain offset, whereas the elastic limit related to the onset of the first plasticity was applied in this work, resulting in a reduced intercept.

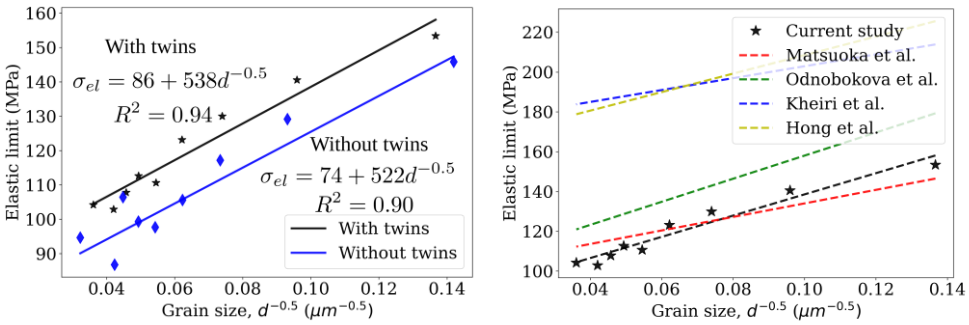


**Fig. 10** (a) Hall-Petch relationship for the case with and without considering twins, (b) comparison of Hall-Petch relationship for 316L stainless steels [35-38]

Fig. 11(a) shows the distribution of the maximum Schmid factor ($m_{max}$) for all grains in the ROI, with an average value of 0.45. To investigate the influence of grain orientations on the identified elastic limits, the values of maximum Schmid factor for

all grains were uniformly classified into 9 groups ranging from its maximum to minimum, where the average values of $m_{max}$ and the elastic limit was calculated in each group, as shown in Fig. 11(b). It is observed that the elastic limit decreases as the maximum Schmid factor increases. This behavior can be attributed to the fact that a higher $m_{max}$ corresponds to a grain orientation that is more favorably aligned for slip activation under the applied loading direction. Consequently, grains with higher $m_{max}$ values tend to reach their plastic deformation threshold at lower stress levels.

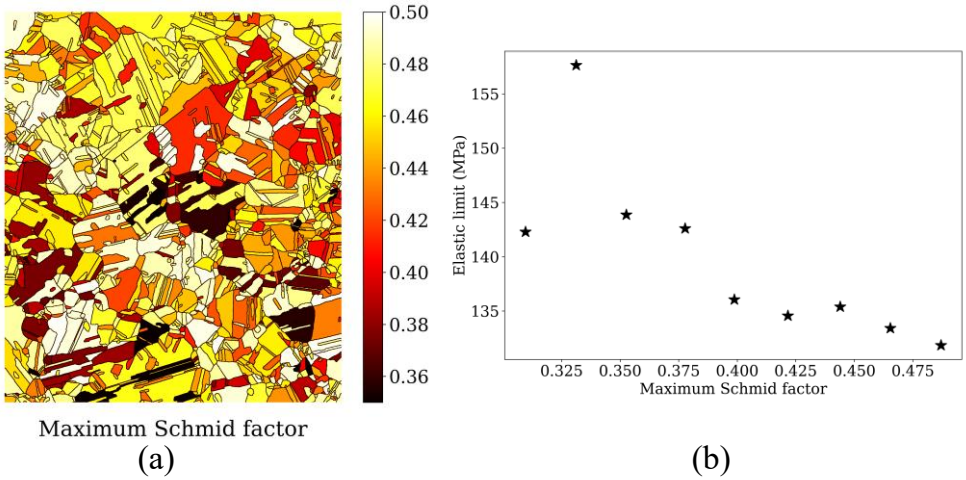


**Fig. 11** (a) Maximum Schmid factor within the ROI, (b) influence of maximum Schmid factor on the elastic limit

According to the Hall-Petch relationship established in Fig. 10(a), the grain scale elastic limit fields for both case are presented in Fig. 12(a) and (c), with a mean and standard deviation of 118±12 MPa and 94±8 MPa, respectively. The elastic limit field considering twins presents a larger mean value, consistent with the description of the Hall-Petch relationship, due to its smaller average grain size. Interestingly, the mean elastic limit determined by the proposed Hall-Petch model for the case with twins is closer to that obtained from the macroscopic curves, which is 124 MPa. This suggests

that the Hall-Petch model considering twins provides a more accurate representation of the elastic limit distribution at the grain scale, which is in good agreement with the macroscopic mechanical behavior.

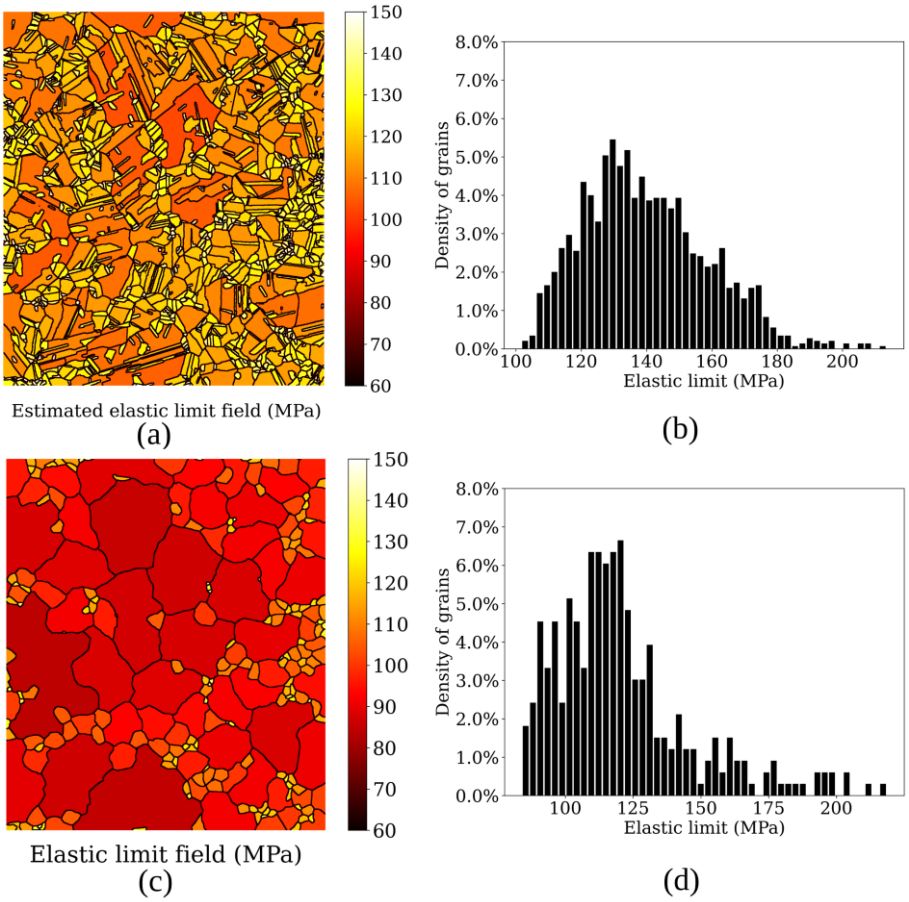


**Fig. 12** Estimated elastic limit fields obtained by the application of Hall-Petch relationship on all grains (a) with and (c) without twins; The histograms of grain-scale elastic limits (b) with and (d) without twins

Plasticity is activated when the resolved shear stress (RSS) on a specific slip system reaches its critical value, known as the critical resolved shear stress (CRSS). For the studied material with FCC structure, it is assumed that only one slip system is predominantly activated at the low macroscopic plastic strain level of the current work (<0.2%). According to Schmid's law, the CRSS is calculated using the following equation:

$$\tau_{CRSS,g} = m_{max,g}\sigma_{el,g}$$

where $m_{max,g}$ and $\sigma_{el,g}$ are the maximum Schmid factor among the 12 possible slip systems and identified elastic limits of grain $g$, respectively.

A statistical analysis was also performed on $\tau_{CRSS,g}$, following the same grain classification based on its size used for analyzing the elastic limit. The results indicate that $\tau_{CRSS,g}$ presents a Hall-Petch relationship, similar to that of the elastic limit, as shown in Fig. 13. The $R^2$ values for the two fitted curves are very close to each other, indicating that both elastic limit and $\tau_{CRSS,g}$ show a Hall-Petch relationship when grain size classification is applied.

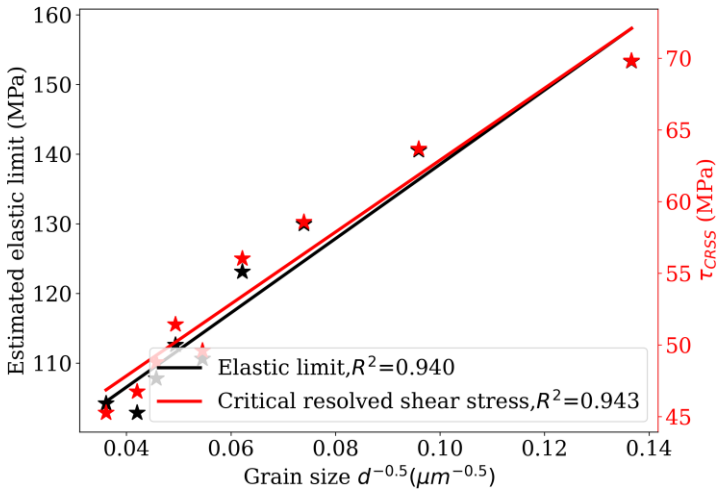


**Fig. 13** Hall-Petch relationship of elastic limit and $\tau_{CRSS,g}$

## Conclusions

In this paper, full-field kinematic measurements are performed on the heat-treated polycrystalline 316L austenitic stainless steel, with a specific focus on the strain fields during uniaxial tensile loading up to approximately 0.2% deformation. The increased grain size induced by heat treatment ensures spatial resolution compatibility with DIC

measurements, facilitating precise measurements at the grain scale. Microstructure observation after electrochemical etching using an optical microscope highlights grains defined by ordinary grain boundaries. On the other hand, grains defined by grain boundary misorientation in EBSD data analysis more distinctly revealed annealing twins resulting from the heat treatment. It is possible to conduct the analysis at the grain scale by segmenting and repositioning these two distinct microstructures obtained through OM and EBSD in the initial DIC configuration. Subsequently, based on the different mechanical responses of the material during elastic and plastic deformation regimes, a method is proposed to identify the activation of plasticity using local strain evolution, thereby obtaining local elastic limits corresponding to the two different microstructures. Furthermore, the identified elastic limits and critical resolved shear stress are statistically analyzed on the classification of grain sizes. The main results are as follows:

(1) The evolution of the full-field strain field shows that strain localizations have occurred before the conventional 0.2% yield strain, mainly at the twin boundaries and triple junctions. Upon entering the hardening stage, the previously occurring strain localization intensifies without new occurrences of localization.

(2) An innovative experiment approach is proposed to identify elastic limits at the grain scale with and without considering annealing twins. This simple method is based on the obtained strain fields, avoiding strong assumptions and quantification of certain microstructure parameters. The average value of the elastic limits for the case considering twins is closer to the value obtained through the macroscopic

stress-strain curve. This suggests the necessity of twins in the identification of the elastic limits.

(3) No clear correlation exists between the identified elastic limits and grain size by direct observation of their distribution. However, a statistical analysis of the classified grain sizes indicates the existence of a Hall-Petch relationship for the case of considering twins, which can be an explanation for verifying such a relationship at the macroscopic scale.

Regarding the perspective, the identified elastic limits based on the local strain evolution need more validation methods, such as the inverse identification methods. Such methods require full-field DIC measurements with a combination of finite element simulations, which will be the scope of future work on polycrystalline aggregates.

**CRediT authorship contribution statement**

Qi Hu: Conceptualization, Methodology, Investigation, Writing–original draft, Writing–review and editing, Visualization. Arnaud Beaurain: Methodology, Investigation. Jean-François Witz: Conceptualization, Methodology, Writing–review and editing. Ahmed El Bartali: Conceptualization, Supervision, Writing–review and editing, Project administration, Funding acquisition. D. Najjar: Conceptualization, Writing–review and editing, Supervision, Project administration.

**Declaration of competing interest**

The authors declare that they have no known competing financial interests or personal relationships that could have appeared to influence the work reported in this

paper.

**Acknowledgements**

The authors gratefully acknowledge the China Scholarship Council (CSC) for funding Qi Hu's PhD thesis and the financial support provided by the RITMEA project (Recherche et Innovation en Transports et Mobilité Écoresponsables et Autonomes). RITMEA is co-financed by the European Union with the European Regional Development Fund, the French state and the Hauts de France Region Council.

**Appendix. Elastic limit calculation with crystallographic computations**

In the main text, a scalar method was applied for the identification of elastic limits, where the calculated stress is a scalar value with the assumption of isotropic Young's modulus. To account for anisotropy effects on the elastic limits, the tensor method using experimental kinematic fields to calculate local stresses with crystallographic computations was applied. According to Hooke's law, the stress tensor is computed as:

$$\underline{\underline{\sigma_{el}}} = \underline{\underline{R^T}}\,\underline{\underline{\underline{\underline{C}}}}\,\underline{\underline{R}}\,\underline{\underline{\varepsilon}}$$

Here, $R$ is the rotation matrix. $C$ is the elastic stiffness tensor. The material under study has an FCC crystal structure, which requires only three independent components for the stiffness tensor: $C_{11}$, $C_{12}$ and $C_{44}$. These constant values vary across different literature. In this study, the optimal values ($C_{11} = 188\ GPa$, $C_{12} = 137\ GPa$, $C_{44} = 88\ GPa$) were determined by minimizing the difference between the stresses calculated using the above formula and the experimentally measured stresses. Afterwards, using the experimentally measured strain components in a 2D case, the stress components at the onset of plasticity correspond to the solution of:

$$\begin{bmatrix} \sigma_{xx} \\ \sigma_{yy} \\ * \\ * \\ * \\ \sigma_{xy} \end{bmatrix} = \underline{\underline{R^T}}\,\underline{\underline{\underline{\underline{C}}}}\,\underline{\underline{R}} \begin{bmatrix} \varepsilon_{xx} \\ \varepsilon_{yy} \\ 0 \\ 0 \\ 0 \\ 2\varepsilon_{xy} \end{bmatrix}$$

In 2D applications, the elastic limit is determined by calculating the von Mises stress at the onset of plasticity, which is expressed as:

$$\sigma_{vm} = \sqrt{\sigma_{xx}^2 + \sigma_{yy}^2 - \sigma_{xx}\sigma_{yy} + 3\sigma_{xy}^2}$$

The result is shown in Fig. A1(a). A comparison with the elastic limits obtained by the scalar method (Fig. A1(b)) reveals similarities in the overall distributions. The mean value of tensor method (124 MPa) equals to the mean value of the scalar method.

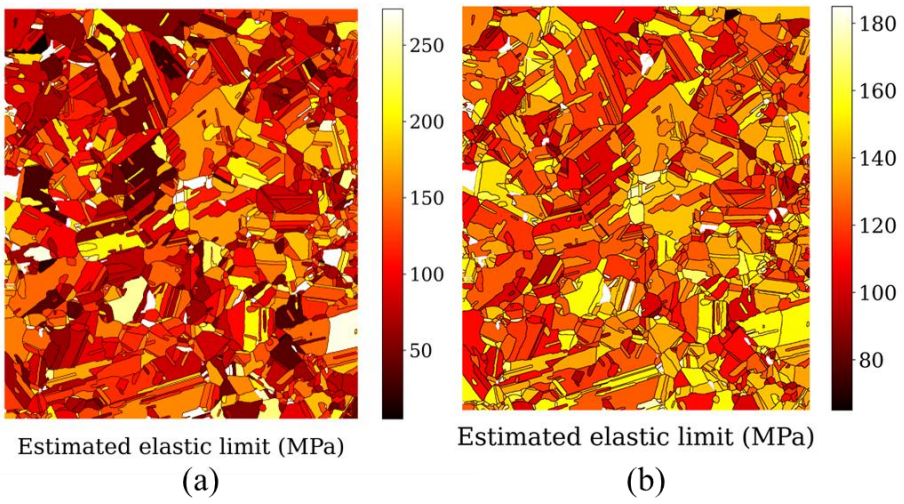


Fig. A1 Elastic limit fields (a) considering the crystal orientation (tensor method), and (b) with isotropic Young's modulus assumption (scalar method)

The elastic limits for grains in Fig. A1(a) were classified using the same size-based criteria as described in the article, and their Hall-Petch relationship was analyzed. As shown in Fig. A2, the scalar method exhibited a higher $R^2$ value, indicating better consistency in describing the Hall-Petch relationship. The difference in the intercept

and slope of the Hall-Petch relationship can be attributed to the selection of the stiffness coefficient values, which require to be further identifying and validating.

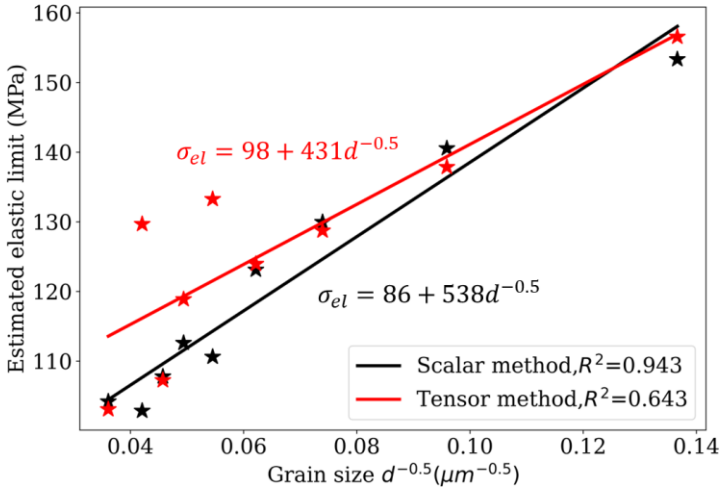


Fig. A2 Comparison of scalar and tensor methods in establishing the Hall-Petch relationship

## References


[1] Zhang HM, Liu J, Sui DS, Cui ZS, Fu MW (2018) Study of microstructural grain and geometric size effects on plastic heterogeneities at grain-level by using crystal plasticity modeling with high-fidelity representative microstructures. Int J Plast 100:69–89. https://doi.org/10.1016/j.ijplas.2017.09.011

[2] Berger A, Witz JF, El Bartali A, Sadat T, Limodin N, Dubar M, Najjar D (2022) Experimental investigation of early strain heterogeneities and localizations in polycrystalline α-fe during monotonic loading. Int J Plast 153:103253. https://doi.org/10.1016/j.ijplas.2022.103253

[3] Agius D, Kareer A, Al Mamun A, Truman C, Collins DM, Mostafavi M, Knowles D (2022) A crystal plasticity model that accounts for grain size effects and slip system interactions on the deformation of austenitic stainless steels. Int J Plast 152:103249. https://doi.org/10.1016/j.ijplas.2022.103249

[4] Vermeij T, Wijnen J, Peerlings RHJ, Geers MGD, Hoefnagels JPM (2024) A quasi-2D integrated experimental–numerical approach to high-fidelity mechanical analysis of metallic microstructures. Acta Mater 264:119551. https://doi.org/10.10

16/j.actamat.20 23.119551

[5] Keller C, Calvat M, Flipon B, Barbe F (2022) Experimental and numerical investigations of plastic strain mechanisms of AISI 316L alloys with bimodal grain size distribution. Int J Plast 153:103246. https://doi.org/10.1016/j.ijplas.2022.103246

[6] Lee HT, Chen JC (1991) Temperature effect induced by uniaxial tensile loading. J Mater Sci 26:5685–5692. https://doi.org/10.1007/BF01130102

[7] Charkaluk E, Seghir R, Bodelot L, Witz JF, Dufrenoy P (2015) Microplasticity in polycrystals: a thermomechanical experimental perspective. Exp Mech 55:741–752. https://doi.org/10.1007/s11340-014-9921-z

[8] Hall EO (1951) The deformation and ageing of mild steel: III discussion of results. Proc Phys Soc Sec B 64(9):747.

[9] Petch NJ (1953) The cleavage strength of polycrystals. J Iron Steel Inst 174:25–28.

[10] Cordero ZC, Knight BE, Schuh CA (2016) Six decades of the Hall–Petch effect–a survey of grain-size strengthening studies on pure metals. Int Mater Rev 61(8):495–512. https://doi.org/10.1080/09506608.2016.1191808

[11] Figueiredo RB, Kawasaki M, Langdon TG (2023) Seventy years of Hall-Petch, ninety years of superplasticity and a generalized approach to the effect of grain size on flow stress. Prog Mater Sci 137:101131. https://doi.org/10.1016/j.pmatsci.2023.101131

[12] Zhu TT, Bushby AJ, Dunstan DJ (2008) Materials mechanical size effects: a review. Mater Technol 23(4):193–209. https://doi.org/10.1179/175355508X376843

[13] Morris Jr JW (2001) The influence of grain size on the mechanical properties of steel.

[14] Bata V, Pereloma EV (2004) An alternative physical explanation of the Hall–Petch relation. Acta Mater 52(3):657–665. https://doi.org/10.1016/j.actamat.2003.10.002

[15] Jiang M, Devincre B, Monnet G (2019) Effects of the grain size and shape on the flow stress: A dislocation dynamics study. Int J Plast 113:111–124. https://doi.org/10.1016/j.ijplas.2018.09.008

[16] Keller C, Hug E, Feaugas X (2011) Microstructural size effects on mechanical properties of high purity nickel. Int J Plast 27(4):635–654. https://doi.org/10.1016/j.ijpl as 2010.08.002

[17] Gu YJ, Stiles CD, El-Awady, JA (2024) A statistical perspective for predicting the strength of metals: Revisiting the Hall–Petch relationship using machine learning. Acta Mater 266:119631. https://doi.org/10.1016/j.actamat.2023.119631

[18] Séchepée I, Dubray C, Velay V, Matsumoto H (2024) Effects of grain size and β fraction on the deformation modes of a Ti-6Al-2Sn-4Zr-2Mo-Si alloy with equiaxed (α+β) microstructures: Slip trace analysis and multiscale simulation of polycrystal plasticity. J Alloys Compd 981:173722. https://doi.org/10.1016/j.jallcom.2024.173722

[19] Moulart R, Rotinat R, Pierron F (2009) Full-field evaluation of the onset of microplasticity in a steel specimen. Mech Mater 41(11):1207–1222. https://doi.org/10. 1016/j.mechmat.2009.07.002

[20] Vermeij T, Verstijnen JAC, Ramirez y Cantador TJJ, Blaysat B, Neggers J, Hoefnagels JPM (2022) A nanomechanical testing framework yielding front&rear-sided, high-resolution, microstructure-correlated SEM-DIC strain fields. Exp Mech 62(9):1625–1646. https://doi.org/10.1007/s11340-022-00884-0

[21] Türkoğlu O, Aydıner CC (2024) An Exploration of grain-averaged stress measurement using partial unloads with in situ microscopic image correlation. Exp Mech 64(5):655–674. https://doi.org/10.1007/s11340-024-01050-4

[22] Hu XB, Liu CH, Wang XH, Jiang C (2024) Full-field quantitative determination of strain and stress partitioning in medium Mn TRIP steels. Met Mater Int 30(4):953–966. https://doi.org/10.1007/s12540-023-01542-3

[23] Avril S, Bonnet M, Bretelle AS, Grédiac M, Hild F, Ienny P, et al. (2008) Overview of identification methods of mechanical parameters based on full-field measurements. Exp Mech 48:381–402. https://doi.org/10.1007/s11340-008-9148-y

[24] Seghir R, Pierron F (2018) A novel image-based ultrasonic test to map material mechanical properties at high strain-rates. Exp Mech 58:183–206. https://

doi.org/10. 1007/s11340-017-0329-4

[25] Madani T, Monerie Y, Pagano S, Pelissou C, Wattrisse B (2018) Identification of heterogeneous elastoplastic behaviors using the constitutive equation gap method. Exp Mech 58:919939. https://doi.org/10.1007/s11340-018-0389-0

[26] Leygue A, Coret M, Réthoré J, Stainier L, Verron E (2018) Data-based derivation of material response. Comput Methods Appl Mech Eng 331:184–196. https://doi.org/10. 1016/j.cma.2017.11.013

[27] Réthoré J, Leygue A, Coret M, Stainier L, Verron E (2018) Computational measurements of stress fields from digital images. Int J Numer Methods Eng 113(12):1810–1826. https://doi.org/10.1002/nme.5721

[28] Dalémat M, Coret M, Leygue A, Verron E (2019) Measuring stress field without constitutive equation. Mech Mater 136:103087. https://doi.org/10.1016/j.mechmat.2019.103087

[29] Bodelot L, Charkaluk E, Sabatier L, Dufrenoy P (2011) Experimental study of heterogeneities in strain and temperature fields at the microstructural level of polycrystalline metals through fully-coupled full-field measurements by digital image correlation and infrared thermography. Mech Mater 43(11):654–670. https://doi.org/10. 1016/j.mechmat.2011.08.006

[30] Dahdah N, Limodin N, El Bartali A, Witz JF, Seghir R, Charkaluk E, Buffiere JY (2016) Damage investigation in A319 aluminium alloy by X-ray tomography and digital volume correlation during in situ high-temperature fatigue tests Strain 52(4):324–335. https://doi.org/10.1111/str.12193

[31] Schindelin J, Arganda-Carreras I, Frise E, Kaynig V, Longair M, Pietzsch T, et al. (2012) Fiji: an open-source platform for biological-image analysis. Nat Methods 9(7):676–682. https://doi.org/10.1038/nmeth.2019

[32] Wang AL, Yan XL, Wei ZJ (2018) ImagePy: an open-source, Python-based and platform-independent software package for bioimage analysis. Bioinformatics 34(18):3238–3240. https://doi.org/10.1093/bioinformatics/bty313

[33] Bouquerel J, Schayes C, Vogt JB (2021) Experimental mesoscopic investigation of the local cyclic plasticity of a non-oriented electrical steel. Mater Sci Eng A

820:141454. https://doi.org/10.1016/j.msea.2021.141454

[34] Sturges HA (1926). The choice of a class interval. J Am Stat Assoc 21(153):65–66.

[35] Odnobokova M, Yanushkevich Z, Kaibyshev S, Belyakov A (2020). On the Strength of a 316L-Type Stainless Steel Subjected to Cold or Warm Rolling Followed by Annealing. Mater 13:2116. https://doi.org/10.3390/ma13092116

[36] Matsuoka Y, Iwasaki T, Nakada N, Tsuchiyama T, Takaki S (2013). Effect of Grain Size on Thermal and Mechanical Stability of Austenite in Metastable Austenitic Stainless Steel. ISIJ Int 53:1224–1230. https://doi.org/10.2355/isijinternational.53.1224

[37] Kheiri S, Mirzadeh H, Naghizadeh M (2019). Tailoring the microstructure and mechanical properties of AISI 316L austenitic stainless steel via cold rolling and reversion annealing. Mater Sci Eng A 759:90–96. https://doi.org/10.1016/j.msea.2019.05.028

[38] Hong C, Lu YH, Zheng HB, Li ZH, Guo GJ (2024). Uniaxial tensile behaviors and Hall-Petch relationship of polycrystalline 316LN stainless steel via molecular dynamics simulation. Comput Mater Sci 244:113195. https://doi.org/10.1016/j.commatsci.2024.113195